Korean J. Chem. Eng., 35(5), 1089-1098 (2018)
DOI: 10.1007/s11814-018-0007-y

pISSN: 0256-1115
eISSN: 1975-7220

Photoreduction of CO_2 into CH_4 using Bi_2S_3-TiO_2 double-layered dense films

Junyeong Kim*, Jeong Yeon Do*, No-Kuk Park, Seung Jong Lee***, Jin-Pyo Hong****, and Misook Kang*,†**

*Department of Chemistry, College of Sciences, Yeungnam University, Gyeongsan, Gyeongbuk 38541, Korea
**School of Chemical Engineering, Yeungnam University, Gyeongsan, Gyeongbuk 38541, Korea
***Institute for Advanced Engineering, 175-28, Goan-ro 51beon-gil, Baegam-Myyeon, Cheoin-gu, Yongin-si, Gyeonggi 17180, Korea
****Korea Electric Power Corporation Research Institute, 105 Munji-ro, Yuseong-gu, Daejeon 34056, Korea
(*Received 20 October 2017 • accepted 11 January 2018*)

Abstract−Nano-sized bismuth sulfide (Bi_2S_3) and titanium dioxide (TiO_2) with the orthorhombic and anatase tetragonal structures, respectively, were synthesized for application as catalysts for the reduction of carbon dioxide (CO_2) to methane (CH_4). Four double-layered dense films were fabricated with different coating sequences—TiO_2 (bottom layer)/Bi_2S_3 (top layer), Bi_2S_3/TiO_2, TiO_2/Bi_2S_3 : TiO_2 (1 : 1) mix, and Bi_2S_3 : TiO_2 (1 : 1) mix/Bi_2S_3 : TiO_2 (1 : 1) mix—and applied to the photoreduction of CO_2 to CH_4; the catalytic activity of the fabricated films was compared to that of the pure TiO_2/TiO_2 and Bi_2S_3/Bi_2S_3 doubled-layered films. The TiO_2/Bi_2S_3 double-layered film exhibited superior photocatalytic behavior, and higher CH_4 production was obtained with the TiO_2/Bi_2S_3 double-layered film than with the other films. A model of the mechanism underlying the enhanced photoactivity of the TiO_2/Bi_2S_3 double-layered film was proposed, and it was attributed in effective charge separation.

Keywords: Double Layered Film, Bismuth Sulfide, Coating Sequence, Carbon Dioxide, Photoreduction, Charge Separation

INTRODUCTION

Carbon dioxide (CO_2) has been cited as the main cause of global warming, although in reality, the global warming value of CO_2 is small compared to that of CH_4 and N_2O [1]. The problem with CO_2 is that, compared to other gases, its emission continues to increase exponentially with time [2], as most fossil fuels that are used as energy sources emit a large amount of CO_2 upon combustion. The International Panel on Climate Change (IPCC) predicted that if atmospheric CO_2 reaches 590 ppm, the mean global temperature will rise by 1.9 °C [3]. Thus, CO_2 is regarded as the major cause of global warming, fueling worldwide research into CO_2 removal. There are at least three routes for reducing atmospheric CO_2, including direct reduction of CO_2 emissions, CO_2 capture and storage (CCS) [4], and CO_2 utilization [5]. Initially, the CCS approach was very popular, but is limited by the environmental risk of leakage and extra energy requirements for gas compression and transportation. During the past decade, the research focus has shifted to the conversion of CO_2 into fuels or valuable chemicals via thermochemical [6], biochemical [7], photochemical [8], and electrochemical [9] routes. Among these methods, the carbon dioxide photochemical transform by solar energy is the most charming prospect as a long-term solution, and can simultaneously address energy and environmental issues. Among the numerous products into which CO_2 can be converted, we focused on methane, which has the highest energy density per gram, in this study [10].

Many catalysts are suitable for the reduction of carbon dioxide. We selected titanium dioxide (TiO_2) from among the known wide-band-gap semiconductors (E_g=3.2 eV) for use as a primary catalyst, because the redox potential of the CO_2 to methane conversion is covered in the energy diagram of the catalyst [11]: $CO_2+8H^++8e^- \rightarrow CH_4+2H_2O$, $E^0=-0.24$ V. Representing the minimum energy between electrons and holes for the carbon dioxide reduction, the electrode potential limits the energy locations of valence band (VB) and conduction band (CB). Additionally, this study is based on the postulate that by increasing the light absorption to the greatest extent possible, the photocatalytic performance can be maximized. Toward this end, many researchers have developed sulfide-based photosensitizer materials such as CuS [12], NiS [13], ZnS [14], CdS [15], Sb_2S_3 [16], and SnS_2 [17] to improve the radiation absorption in the visible area to achieve enhanced photocatalytic activity. These catalysts provide slightly improved catalytic activity relative to the low activity of pure TiO_2. Bi_2S_3, which is used as a photosensitizer material in this study, has previously been used as a photocatalyst because of its excellent gas absorption ability and optical activity [18,19].

During materials synthesis, the synthesized nanomaterials are randomly mixed with another material which leads to decreased uniformity and reduced reusability of the catalyst [20]. Recently, a photocatalyst having a uniform structure such as a core@shell has been reported; in particular, the core@shell structure composed of a metal oxide core and a metal sulfide shell enhances light absorption and a stable photocatalyst performance due to an effective separation between excited photoelectrons and holes, respectively [21]. However, it is not easy to make the core@shell structure perfect and reproducible. Therefore, we attempted to fabricate two types

†To whom correspondence should be addressed.
E-mail: mskang@ynu.ac.kr

of powder photocatalysts in film form by using double layer coating method in order to have an effective separation between excited photoelectrons and holes as like core@shell function. Six double-layered dense films were thus fabricated with different coating sequences (bottom layer/top layer=TiO_2/TiO_2, Bi_2S_3/TiO_2, Bi_2S_3/Bi_2S_3, TiO_2/Bi_2S_3, TiO_2/Bi_2S_3 : TiO_2 (1 : 1) mix, and Bi_2S_3 : TiO_2 (1 : 1) mix/Bi_2S_3 : TiO_2 (1 : 1) mix) and applied in the photoreduction of CO_2 to CH_4. Furthermore, a mechanism for the enhancement of the photoactivity over the double-layered film was proposed.

EXPERIMENTAL

1. Preparation of Catalysts

Bi_2S_3 and TiO_2 powder were prepared by conventional sol-gel treatment. Bismuth chloride ($BiCl_3 \cdot 6H_2O$, 99.99%, Junsei Chem. Co., Japan) and sodium thiosulfate ($Na_2S_2O_3 \cdot 5H_2O$, 99.99%, Junsei Chem. Co., Japan) were used as the Bi and S precursors, respectively, and absolute ethanol (C_2H_5OH) was used as the solvent. These reagents were mixed in a molar ratio of Bi : S=2 : 3 in absolute C_2H_5OH and stirred for 1 h, and the solution was heat-treated for 30 minutes at 80 °C. The obtained precipitate was washed, dried at 60 °C overnight, and finally thermal-treated at 250 °C for 2 h in argon to induce crystal formation, finally affording dark grey Bi_2S_3. Titanium tetraisopropoxide ($Ti[OCH(CH_3)_2]_4$, 99.95%, Junsei Chem. Co., Japan) and absolute C_2H_5OH were used as the Ti precursor and solvent, respectively. First, 1.0 mL of titanium tetraisopropoxide was slowly added dropwise into absolute C_2H_5OH, and continued by the addition of 6.0 mL distilled water. The solution was homogeneously stirred for 2 h, and then followed by evaporation at 80 °C. The resulting powder was thermally treated at 500 °C for 5 h to induce crystal formation, finally affording white anatase-structured TiO_2.

To fabricate the double-layered films, pastes containing different ratios of Bi_2S_3 and TiO_2 were prepared as follows: 5.0 g of powder (Bi_2S_3, TiO_2, or a 1 : 1 molar ratio mixture of TiO_2 and Bi_2S_3) was added to a mixture of 60 mL of absolute C_2H_5OH, 60 mL of Triton X-100, and 60 mL of ethylene glycol in an agate mortar with grinding for 40 min. A conventional glass plate was ultrasonically cleaned in DI water for 30 minutes and dried in an oven. The film was fabricated by coating the paste on the glass substrates (taped with dimensions of 5.0 mm in the horizontal direction×8.0 mm in the vertical direction) by a general squeeze-printing method using a 30-micron thickness tape. After the coated glass substrates were dried at 100 °C for 10 min, this film was thermal-treated at 450 °C for 1 h under flowing inert gas and eventually became the bottom layer. The cross section of the fabricated film was cut, and the film thickness was confirmed by SEM photograph. In the second step, the forming method for TiO_2, Bi_2S_3, or TiO_2 and Bi_2S_3 mixed pastes of top layer was the same as the manufacturing method of bottom paste, but it reduces the amount of powder to 1/100, so that here, the upper layer was thinly coated as much as possible in order to form an interface between bottom and top. The top paste was also coated in one layer on the bottom layer in a squeeze-printing method (use of 50-micron thickness tape). After drying at 100 °C for 10 min, the final films were also thermal-treated at 450 °C for 2 h under flowing inert gas. As a result of confirming the film thickness in the same manner, there was almost no change compared to the bottom thickness. For comparison purposes, six types of double-layered films were fabricated: TiO_2/TiO_2, Bi_2S_3/TiO_2, Bi_2S_3/Bi_2S_3, TiO_2/Bi_2S_3, TiO_2/Bi_2S_3 : TiO_2 (1 : 1) mix, and Bi_2S_3 : TiO_2 (1 : 1) mix/Bi_2S_3 : TiO_2 (1 : 1) mix.

2. Characterizations of Catalysts

The Bi_2S_3 and TiO_2 particles were characterized using X-ray diffraction (30 kV, 30 mA, MPD, PANalytical) with nickel-filtered Cu-Kα radiation, transmission electron microscopy (TEM, H-7600, Hitachi), energy-dispersive spectrometry with element mapping (EDS/mapping, EX-250, Horiba), X-ray photoelectron spectroscopy (XPS, AXIS Nova, Kratos Inc.), and diffuse-reflectance UV-visible spectra recorded on a Cary 500 spectrometer. Photocurrent density (Compact Stat, IVIUM STAT Tech.) and photoluminescence (PL, 300 nm, He-Cd laser source, Perkin Elmer) spectroscopy were substituted.

3. Catalytic Performances on Carbon Dioxide Photoreduction

The photoreactor was designed for a CO_2 reduction reaction (Fig. 1). A film type catalyst was located in the middle portion of the reactor. The total volume of a rectangular quartz cell reactor was 16.0 mL. A thick quartz glass window cover of 1.0 mm was located on the top of reactor, and a 6.0 $W \cdot cm^{-2}$ mercury lamp of 365 nm was used to enable the effective transfer of radiation. The leakage in reactor was checked at atm. pressure over several hours with purging He as the carrier gas. The CO_2 concentration was controlled by dilution with helium gas. The reaction temperature and pressure were maintained at 40 °C and 1.0 atm, respectively. Just before the start of the experiment, the reactor was stabilized for 1 h with a mixture of CO_2 and He. The CO_2 : H_2O=1 : 4 ratio was maintained. During photocatalysis, the product mixtures were ejected off-line using a gas syringe (Agilent, 250 μm) with the same volume and determined using a gas chromatograph (GC, iGC7200, Donam Co., Korea) combined with a flame ionization detector (FID) and a thermal conductivity detector (TCD). The ejected gaseous products were moved to a TCD detector (Carboxen 1000 column, Young Lin Instrumentals Co., Korea) for analysis of light gases (H_2, O_2, CO, and CO_2), and then transferred to an FID detector to analyze C_1-C_3 light hydrocarbons and oxygenated compounds such as methanol (CH_3OH), acetaldehyde (CH_3COOH), and for-

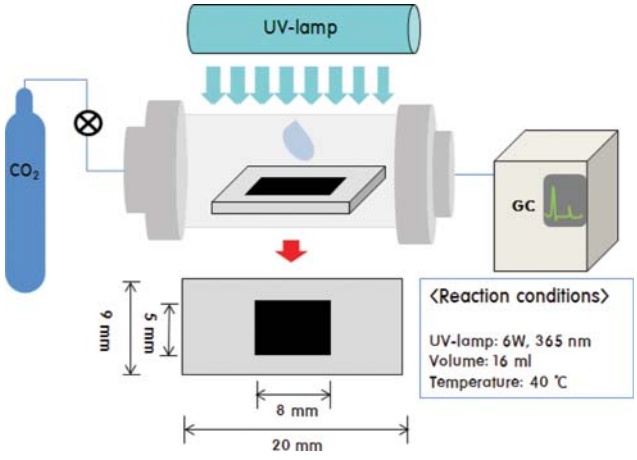

Fig. 1. Batch-type reactor designed for the CO_2 photoreduction.

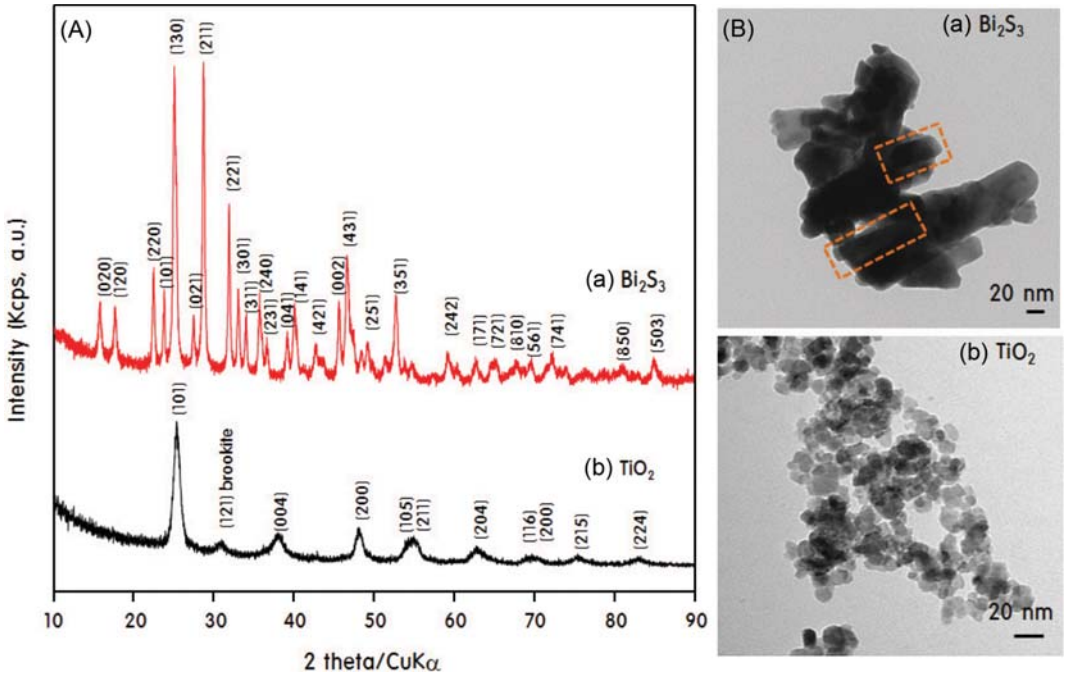

Fig. 2. XRD patterns (A) and TEM images (B) of nano-sized Bi_2S_3 and TiO_2 particles.

mic acid (HCOOH).

RESULTS AND DISCUSSION

1. Physicochemical Properties of the Synthesized Bi_2S_3 and TiO_2 Powders

Figs. 2(A) and (B) show the X-ray diffraction (XRD) patterns and TEM images of the Bi_2S_3 and TiO_2 powder, respectively. The XRD spectrum of the TiO_2 powder (Fig. 2(A)) shows peaks at 2θ values (plane) of 25.3° (101), 38.0° (004), 48.2° (200), 54.0° (105), 63° (211), and 68.0° (204), indexed to the tetragonal-phase anatase structure (JCPDS No. 001-0562); the broad peaks indicate that the crystallite size is small. As a reference point, a low-intensity peak of brookite TiO_2 (121 diffraction plane) was present. Maybe, although the crystallization temperature was low during the synthesis, brookite could still have been formed at relatively low temperatures. However, the amount of brookite formed was very small, and the optical activity of the brookite structure was generally lower than that of the anatase structure; thus, the presence of brookite was ignored in this study. For Bi_2S_3, XRD peaks corresponding to the (020), (120), (220), (101), (130), (021), (221), (301), (311), (240), (231), (041), (141), (421), (002), (431), (251), (351), (242), (171), (721), (810), (561), (141), (850), and (503) crystal planes were observed, indicating the orthorhombic phase (JCPDS No. 001-0320). The mean crystallite sizes were calculated from the peaks assigned to the (101) plane of anatase TiO_2 and the (130) plane of Bi_2S_3 according to the Scherrer formula [22]; the values calculated for the TiO_2 and Bi_2S_3 crystallites were 9.25 and 17.00 nm, respectively. The TEM image of the TiO_2 sample (Fig. 2(B)) showed spherical nanoparticles with a size of less than 10 nm. Bi_2S_3 adopted a rod-like morphology, as illustrated in the boxed regions of the photograph, and the crystal dimensions were estimated to be approximately 80-120 nm (length) by 40 nm (width).

The oxidation states of the components of the TiO_2 and Bi_2S_3 particles were quantitatively analyzed by XPS, as shown in the typical survey and high-resolution spectra in Fig. 3. The binding energies of the elements Bi and S overlapped between 156 and 166 eV in Bi_2S_3. The peaks at binding energies of 158.3 and 163.6 eV were assigned to the Bi $4f_{7/2}$ (highest occupied molecular orbital) and $4f_{5/2}$ (lowest unoccupied molecular orbital) states, corresponding to Bi^{3+} in the Bi_2S_3 sample [23], and these peaks were again split into two peaks at 159.5 and 164.5 eV, which are attributed to Bi_2O_3 itself. These results confirmed that a small amount of oxygen that was not substituted by sulfur remained in Bi_2S_3. The broad peaks for $S2p_{3/2}$ and $2p_{1/2}$ at binding energies of 160.9 and 161.8 eV assigned to sulfide were observed in Bi_2S_3. The peaks of the Ti $2p_{1/2}$ and $2p_{3/2}$ spin-orbital splitting photoelectrons for anatase TiO_2 were located at 464.2 and 458.5 eV binding energies, respectively, and were attributed to six-coordinated octahedral Ti^{4+} [24]. The difference between the two bands was 5.7 eV, and the peak positions were typical for anatase crystals. The O1s region was decomposed into two contributions, Ti-OH (529.2 eV) and Ti-O (530.7 eV). The Ti-OH/Ti-O ratio determined from the O 1s peaks was greater than 3.0. Generally, a high contribution from the Ti-OH peak means that the TiO_2 particles are hydrophilic [25].

To semi-quantitatively analyze the elemental composition of the TiO_2 and Bi_2S_3 particles, elemental mapping imaging and energy dispersive X-ray spectroscopy were used and the results are shown in Fig. 4(A) and (B), respectively. On the basis of the elemental mapping image, it was confirmed that all of the elements, Bi, S, Ti, and O, were uniformly dispersed. EDS analysis revealed the presence of Bi, S, Ti, and O in pure Bi_2S_3 and TiO_2, with Bi : S and Ti : O atomic ratios of 42.52 : 57.48 (about 2 : 2.7) and 21.93 : 78.08 (about 1 : 2.1), respectively; these values are close to the stoichio-

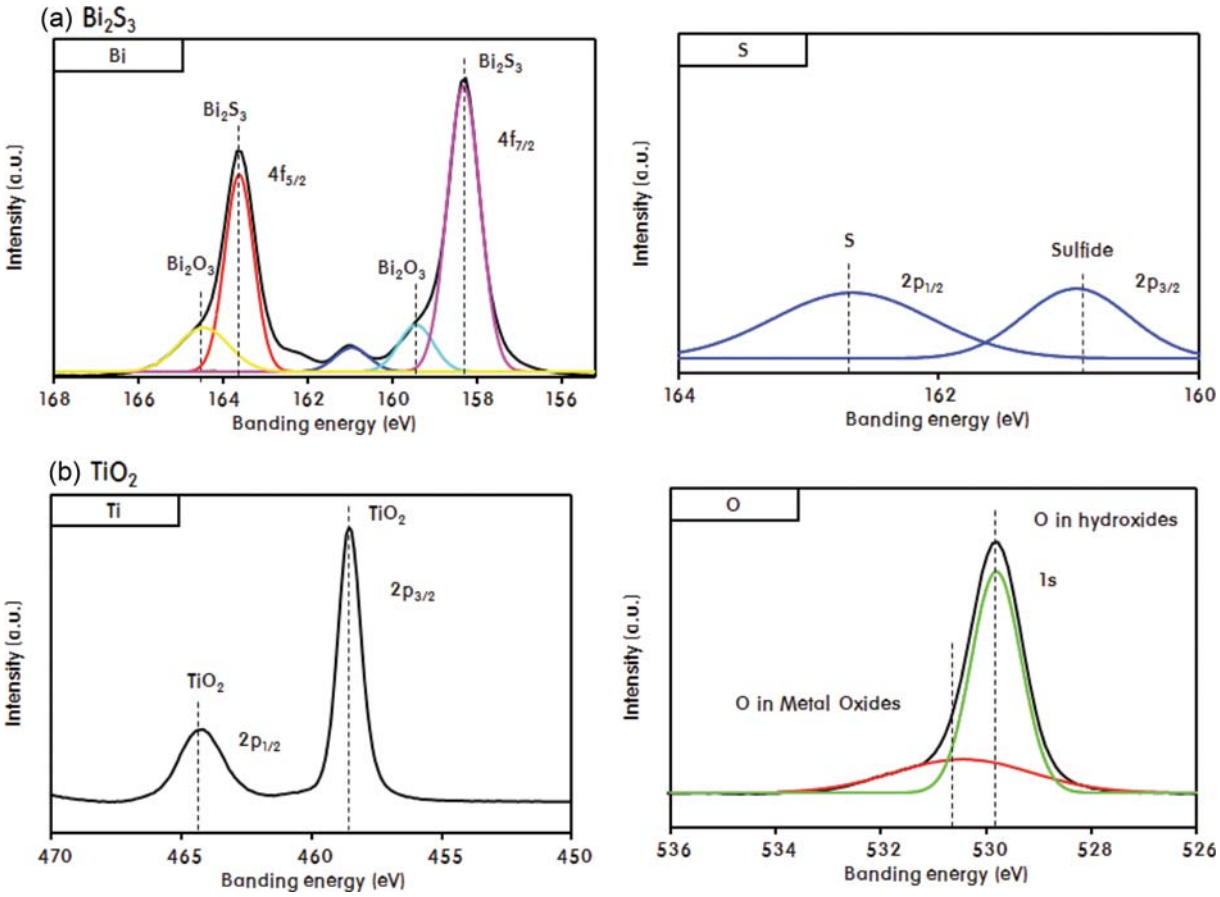

Fig. 3. High-resolution XPS spectra of TiO_2 and Bi_2S_3 particles.

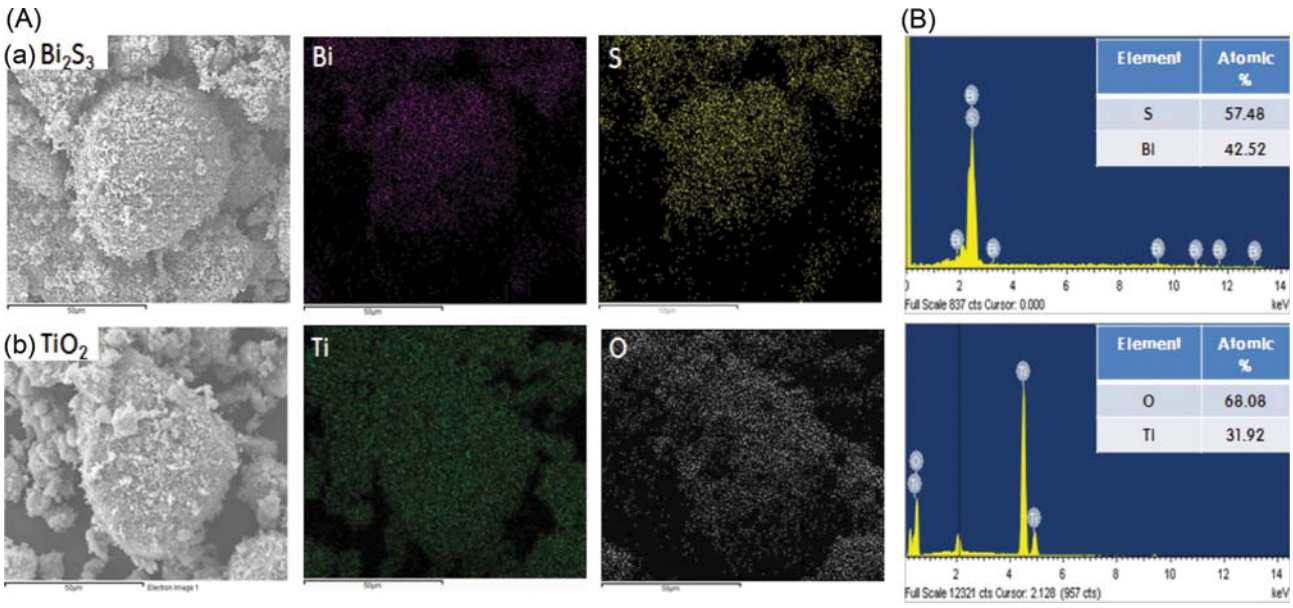

Fig. 4. Elemental mapping imaging (A) and energy dispersive X-ray spectra (B) of TiO_2 and Bi_2S_3 particles.

metric mole fractions of Bi_2S_3 (Bi : S=2 : 3) and TiO_2 (Ti : O=1 : 2).

The catalytic performance is strongly related to the adsorbing abilities of the reactants during a chemical reaction. The larger the surface area, the greater the adsorbing ability of the reactant, and consequently, the catalyst performance increases [26]. Fig. 5 shows the 77 K N_2 adsorption-desorption isotherms for Bi_2S_3 and TiO_2.

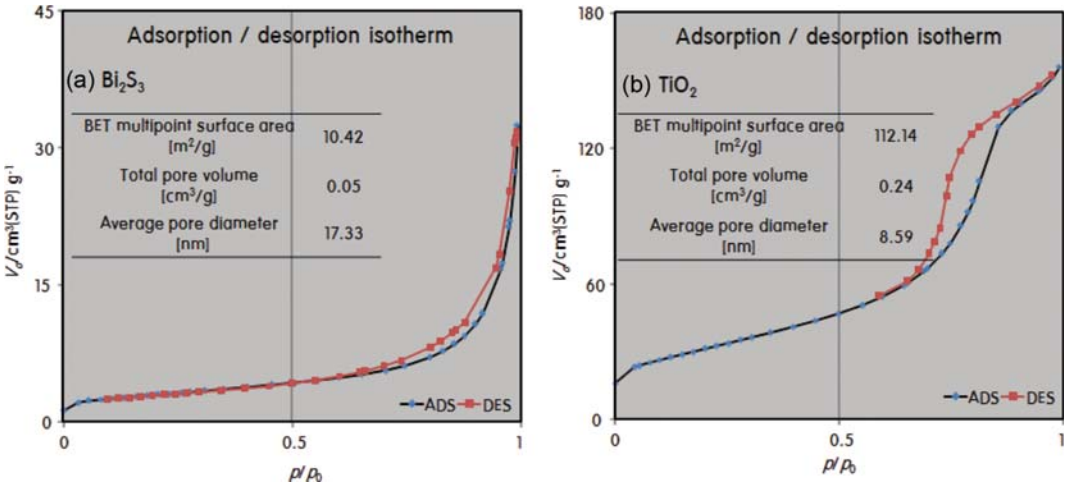

Fig. 5. Adsorption-desorption isotherms of N_2 at 77 K for Bi_2S_3 and TiO_2 particles.

Using Kelvin's equation [27], the mean pore diameter (D_p) can be calculated from $D_p=4V_T/S$ as a function of the relative pressure (P/P_0), where S is the BET surface area and V_T is the total volume of the pores. According to the IUPAC classification system [28], the isotherm for pure Bi_2S_3 was type II, indicative of particles with no pores. Additionally, the specific surface area of Bi_2S_3 was very small ($10\ m^2 \cdot g^{-1}$) because of the large particles. Generally, the specific surface areas of regular particles are strongly correlated to the particle size, with smaller particle size being associated with larger surface area [29]. Hysteresis loops were observed at higher relative pressures in the type IV isotherm (IUPAC classification) of the TiO_2 nanoparticles, possibly indicating the presence of bulk mesopores between the TiO_2 particles; the mean specific surface area and pore diameter were $112.14\ m^2 \cdot g^{-1}$ and 8.58 nm, respectively.

2. Catalytic Performance of Photoreduction of CO_2 into CH_4 on the Fabricated Double-layered Dense Films

The double layered films were fabricated as described in the experimental section. Six types of double-layered films, TiO_2/TiO_2, Bi_2S_3/TiO_2, Bi_2S_3/Bi_2S_3, TiO_2/Bi_2S_3, TiO_2/Bi_2S_3 : TiO_2 (1 : 1) mix, and Bi_2S_3 : TiO_2 (1 : 1) mix/Bi_2S_3 : TiO_2 (1 : 1) mix, were fabricated. Fig.

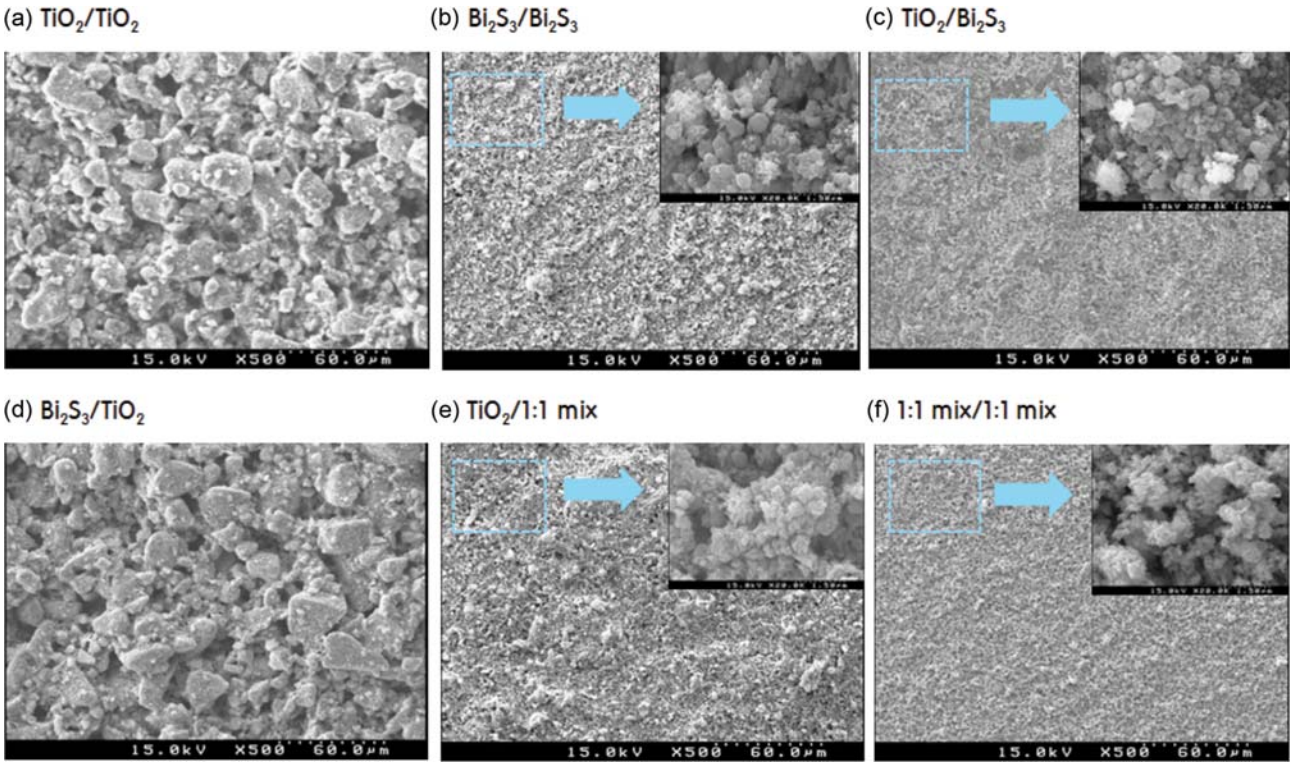

Fig. 6. Top-view SEM images of the surfaces of the six double-layered films, TiO_2/TiO_2, Bi_2S_3/TiO_2, Bi_2S_3/Bi_2S_3, TiO_2/Bi_2S_3, TiO_2/Bi_2S_3 : TiO_2 (1 : 1) mix, and Bi_2S_3 : TiO_2 (1 : 1) mix/Bi_2S_3 : TiO_2 (1 : 1) mix.

6 shows the top-view SEM image of the sample surfaces. There were differences of the roughness and the particle morphology of the surfaces of the films. The surfaces of the TiO_2/TiO_2 and Bi_2S_3/TiO_2 films showed a high degree of aggregation of the particles, and large pores were formed between the agglomerated particles, which facilitated gas adsorption during the reaction. In contrast, for the other films, the particles were uniformly dispersed and formed a dense surface. The surfaces of the layers of the TiO_2/Bi_2S_3 and Bi_2S_3 : TiO_2 (1 : 1) mix/Bi_2S_3 : TiO_2 (1 : 1) mix were very tightly connected to each other.

Before discussing the photocatalytic performances of the six types of double-layered films, the mechanism of CO_2 photoreduction should be briefly discussed. The photoreduction of CO_2 consists of three processes: (1) production of protons from the photodecomposition of H_2O, (2) production of CO or C radicals from the photocleavage of CO_2, and (3) production of CH_4 from photoreaction between the proton and the CO (or C) radical [30]. The photogenerated electrons on the semiconductor surfaces arising from UV radiation bring to the reduction of CO_2, offering CO_2^- radicals, since oxidation occurs via reaction between the holes and the adsorbed H_2O molecules. The intermediate photogenerated species take different reactions, offering CO and CH_4. Based on this mechanism, various species may be generated during the photocatalytic CO_2 reduction reaction. Generally, CH_4, CH_3OH, CO, and CH_3COOH are produced; the selectivity of the reaction towards particular species varies depending on the catalyst used. Notably, we observed almost no CH_3OH or CH_3COOH in the products, and mainly CH_4 and CO were produced. The distributions of the products generated during the CO_2 photoreduction reaction on the six types of double-layered films are shown in Fig. 7. Here, the film thicknesses were fixed as equal as possible to exclude the influence of the activity on the amount of catalyst. The film thicknesses of TiO_2/TiO_2, Bi_2S_3/TiO_2, Bi_2S_3/Bi_2S_3, TiO_2/Bi_2S_3, TiO_2/Bi_2S_3 : TiO_2 (1 : 1) mix, and Bi_2S_3 : TiO_2 (1 : 1) mix/Bi_2S_3 : TiO_2 (1 : 1) mix were 24.0, 24.4, 24.5, 24.5, 23.5, and 24.5 μm, respectively. More specifically, no separation surface between the bottom and the top layers was found in all films, and the thickness of the double layered-film was not different from that of the bottom layer. It was expected that the top layer would be coated very thinly as we intended (as already mentioned in the introduction and preparation section). Only a few cloud lines were seen in the top layer presumably the coated double layer. When these films were used as catalysts, the carbon dioxide photoreduction performance decreased in the following order: TiO_2/Bi_2S_3>TiO_2/Bi_2S_3 : TiO_2 (1 : 1) mix>Bi_2S_3 : TiO_2 (1 : 1) mix/Bi_2S_3 : TiO_2 (1 : 1) mix>TiO_2/TiO_2>Bi_2S_3/TiO_2>Bi_2S_3/Bi_2S_3. Unusually, the relative rates of CH_4 and CO production were similar for all films: the ratio of CH_4 to CO produced was constant at 3 : 1. We predicted that this was because CO was formed as an intermediate, and subsequently reduced to the final CH_4. Thus, if the reaction time or the amount of the catalyst is increased, the yield of CH_4 may increase.

The results of the photocatalytic reduction of CO_2 into CH_4 over the double-layered films using H_2O vapor are shown in Fig. 8. Photocatalytic reduction of CO_2 over the double-layered films produced relatively low yields of CH_4 when the films with Bi_2S_3 on the bottom layer (Bi_2S_3/Bi_2S_3 and Bi_2S_3/TiO_2) were used. On the other hand, the TiO_2/TiO_2 film and the films with mixed Bi_2S_3 and TiO_2 layers exhibited moderate CO_2 reduction performance. The TiO_2/Bi_2S_3 film with TiO_2 as the bottom layer and Bi_2S_3 as the top layer showed the best performance: the maximum CH_4 yield was 35.2 $\mu mol \cdot g_{cat}^{-1} L^{-1}$ after 10 h. Based on these results, it is proposed that the TiO_2/Bi_2S_3 film more effectively hinders the recombination between the generated electron and hole, which limits the photoactivity, compared to other films. Unfortunately, this CH_4

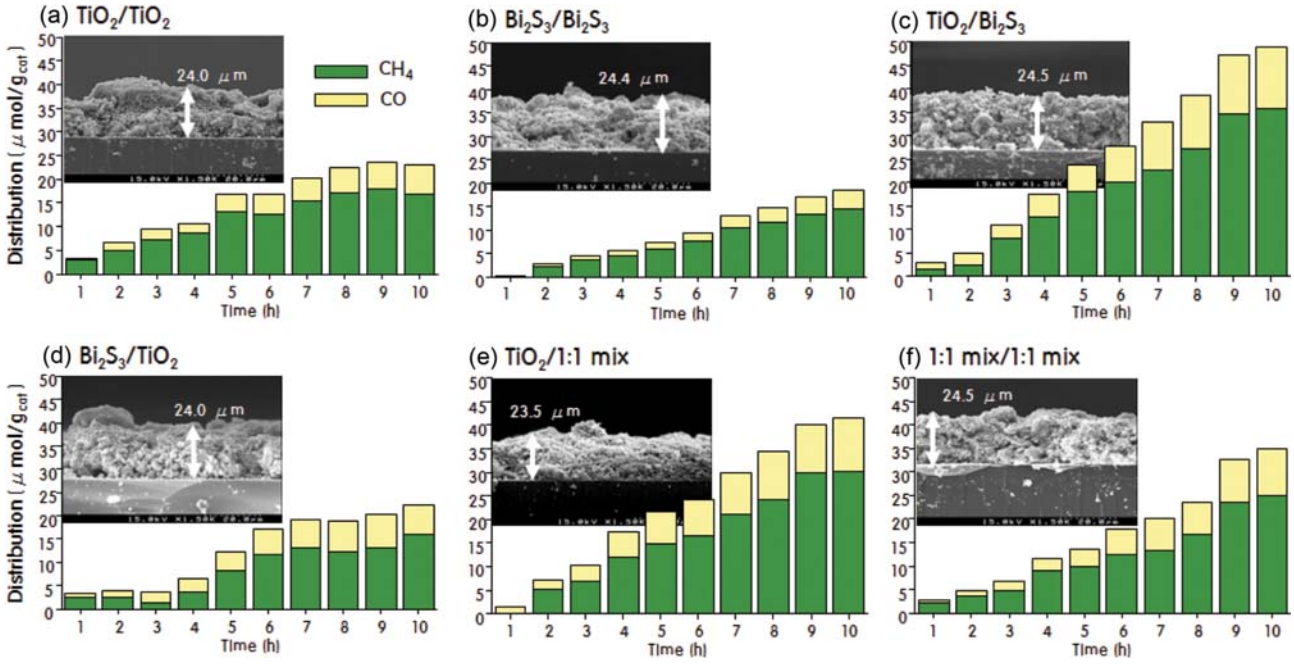

Fig. 7. Product distributions during CO_2 photoreduction over the double-layered films.

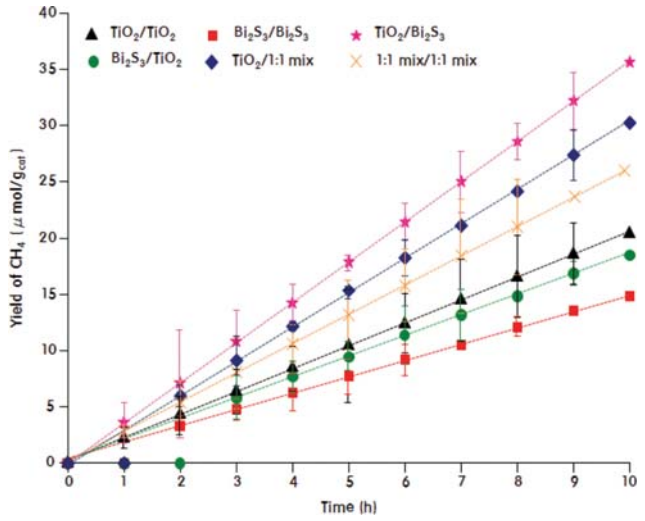

Fig. 8. Photocatalytic performance for CO_2 photoreduction into CH_4 over the double-layered films.

yield is the lowest compared to the results presented in our previous studies [12,13,25,31]. As a first example, in double layered CuS/TiO_2 and NiS/TiO_2 films fabricated using CuS or NiS photosensitizers, about 53 μmol·$g_{cat}^{-1}L^{-1}$ of CH_4 was generated after 8 and 10 h, respectively [12,13]. This was related to the inherent properties of the doped metals: the Ni and Cu ingredients in NiS and CuS have many electrons in the valence band, which facilitates the transfer of electrons to CO_2. Moreover, these metal ingredients have good hydrogen spillover capacity (greater in Cu than Ni) [32], and facilitate the transfer of hydrogen atoms by decomposing water and the formation of CH_4 by bonding well with CO_2 [33]. Note that the doped metal ingredients which are mentioned in this study are not independent metallic nanoparticles, even though a number of papers on CO_2 photoreduction on noble metal nanoparticles (or the loaded) such as Ag, Au, or Pt have been recently published, and additionally the reports confirmed that their photocatalytic performance was improved due to both the electron-trapping and surface plasmon resonance (SPR) effects of noble metal nanoparticles [34,35]. On the other hand, the Bi ingredient in Bi_2S_3 used in this study also has electrons in the valence band, which facilitates electron transfer to CO_2. However, Bi ingredient has less hydrogen spillover capacity compared to Cu or Ni elements, making the transfer of hydrogen atoms difficult, which seems to have inhibited the reduction of CO_2 into CH_4. As a second example, a double layered Cu-TiO_2/TiO_2 film in our previous studies produced 175 μmol·$g_{cat}^{-1}L^{-1}$ of CH_4 via CO_2 photoreduction during 8 h. This result represented a greatly improved CO_2 reduction performance compared to catalysts using CuS on the top layer. In this case, the Cu dopant increased the electron-hole separation in the Cu-TiO_2 particles, and the band gap of Cu-TiO_2 was larger than the band-gap of CuS; thus, recombination between electrons and holes was expected to be suppressed during CO_2 photoreduction [25]. As a final example, Bi-TiO_2 powder was used as a photocatalyst [31] for CO_2 reduction. In the case of 5 mol% Bi-TiO_2, which showed the greatest increase in photocurrent, CH_4 production was significantly improved to 34,000 μmol·$g_{cat}^{-1}L^{-1}$ after 8 h. In this example, the catalyst was used in powder form, which is quite different from the double layer films used in the current study. That is, most of the surface area of the particles could be accessed in the powder catalyst, and the electron-hole separation in the particles due to the Bi dopant could be improved. For these reasons, many of the studies mentioned used metal sulfide catalysts in the form of powder particles. Metal sulfides have a small band gap and can easily absorb light in the visible region. In particular, when metal sulfide/metal oxide [33] or metal sulfide/metal sulfide [36] heterojunction powder types are used, the separation between the electron and the hole between the interfaces can be easily achieved, and thus the photocatalytic activity can be sustained for a long

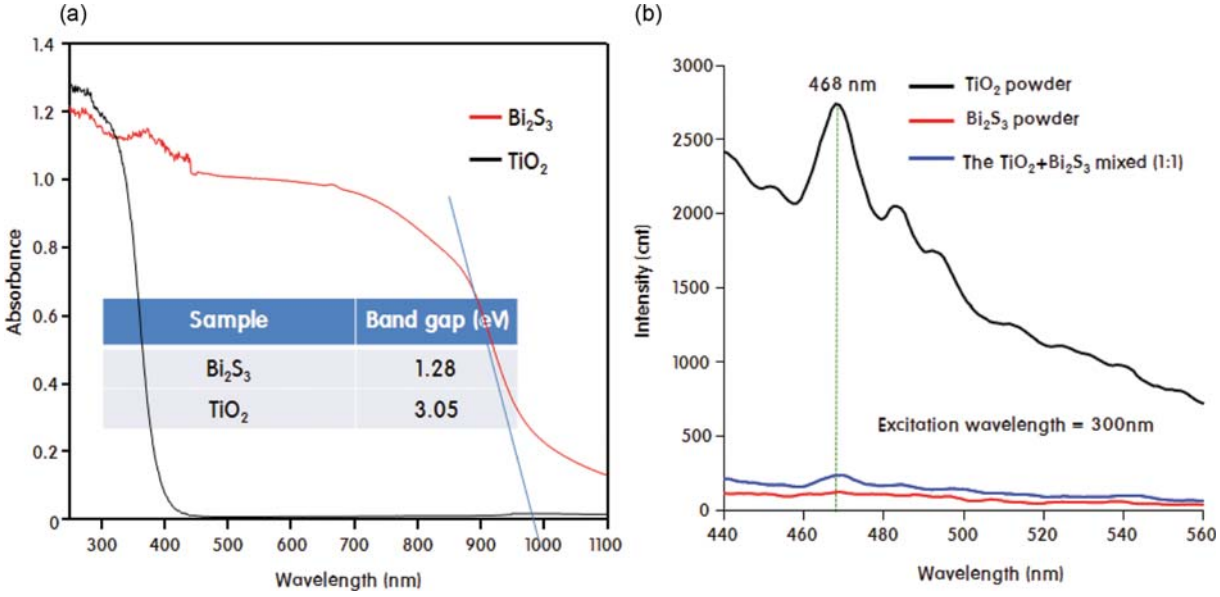

Fig. 9. UV-visible absorption (a) and photoluminescence (b) spectra of the prepared TiO_2 and Bi_2S_3 particles.

time. Nevertheless, we believe that the double layered film type catalysts introduced in this study are essential in terms of catalyst technology development, because film-based catalysts offer advantages in both environmental aspects, such as recyclability and reuse, and industrial aspects important to commercialization of the product, which are rarely used as simple powders on the industrial scale. Furthermore, on the basis of these results, we could add the following conclusion: even with the same metal species, the catalytic performance perhaps vary depending on many factors as like the counter ion species (S, N, or O), the amount of metal introduced, and the form of the catalyst (powder or film).

3. Correlation between Spectroscopic Properties and Optical Activity of Film Catalysts

Spectroscopic studies were conducted to determine the origin of the improved optical activity of the TiO_2/Bi_2S_3 film in the photoreduction of CO_2 as compared to the other films. Fig. 9 shows the UV-visible (A) and PL spectra (B) of the prepared TiO_2 and Bi_2S_3 powders. For anatase TiO_2, as shown in Fig. 9(a), a band was clearly showed around 400 nm after extrapolation, which resembles absorption bands reported elsewhere [37]. On the other hand, for Bi_2S_3, a broad absorption was observed over the entire region; notably, the maximum was observed at 970 nm [38]. The optical band-gap was determined by using the energy-wavelength relation, $E_g=hc/\lambda$, where h is Planck's constant, c is the velocity of light, and λ is the wavelength estimated from the absorption tail; the band-gaps of TiO_2 and Bi_2S_3 were estimated to be 3.05 and 1.28 eV, respectively. Generally, the band-gaps of semiconductors are strongly connected to the absorbed wavelengths: a semiconductor that absorbs higher wavelength has lower band gap. Thus, the observed absorption of Bi_2S_3 is favorable for enhancing the rate of utilization of solar energy. PL measurements are typically engaged to investigate the separation efficiency of the photo-induced electron-hole pairs and the charge carrier lifetime of semiconductor particles. Fig. 9(b) shows the respective PL spectra of the prepared TiO_2 and Bi_2S_3 powders, and of the mixed powder sample comprising TiO_2 and Bi_2S_3. Generally, the PL intensity increases with an increase in the number of emitted electrons as a result of recombination between the excited electrons and holes and the consequent decrease in the photoactivity [39]. Thus, there is a close correlation between PL intensity and photocatalytic activity. Notably, the PL intensity declines significantly when a metal particle captures excited electrons or exhibits conductivity, which is referred to as relaxation. Generally, substances emit at characteristic wavelengths; for the purpose of comparison, we observed excitations at the same wavelength of 300 nm in all of the samples, and the PL curves were observed at 468 nm. The PL intensity of Bi_2S_3 was significantly lower than that of TiO_2, whereas that of the mixed sample was higher than that of pure Bi_2S_3, which was attributed to the oxygen vacancies in the mixed sample.

The valence band spectra were constructed from the XPS study of the TiO_2 and Bi_2S_3 powders in order to further understand the electron transfer energy during CO_2 photoreduction, as shown in Fig. 10(a). The broad peak was identified as the valence band of the powders, and the valence bands of TiO_2 and Bi_2S_3 were observed at 0.94 and 2.72 eV, respectively. Based on the results obtained from the UV analysis and the valence band energy determined from the XPS spectroscopic measurement, an energy diagram was proposed for TiO_2 and Bi_2S_3, as shown in Fig. 10(b). Compared to pure TiO_2, Bi_2S_3 had a smaller band-gap, and the CB and VB potential energies of Bi_2S_3 were located at slightly higher levels than those observed for TiO_2. Moreover, when TiO_2/Bi_2S_3 is fabricated in the form of a double-layered film, the electrons are predominantly emitted from the VB to the CB of Bi_2S_3, which has a smaller band-gap, and the emitted electrons are then transferred to the CB of TiO_2, resulting in decreased recombination of the electrons and holes for the TiO_2/Bi_2S_3 double-layered film.

Fig. 11(a) exhibits the classical real-time photocurrent response of three films TiO_2/TiO_2, Bi_2S_3/Bi_2S_3, and TiO_2/Bi_2S_3 during on-off light cycles. In semiconductor systems, when irradiation provides energy exceeding the band-gap of the semiconductor, the elec-

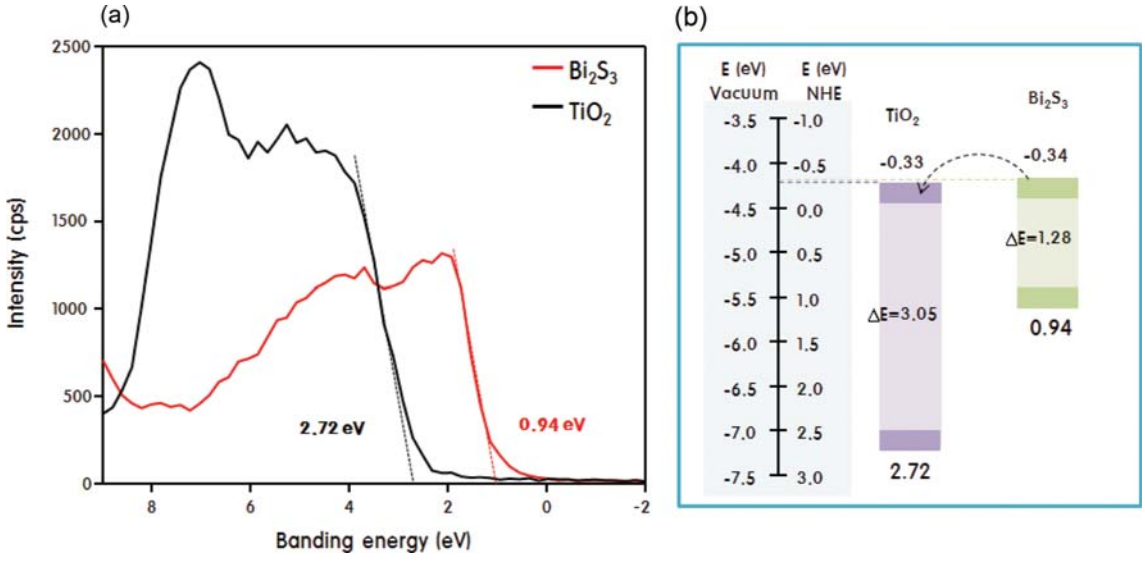

Fig. 10. Valence band spectra determined from the XPS study of the TiO_2 and Bi_2S_3 particles (a) and electron transfer energy diagram for TiO_2 and Bi_2S_3 particles (b).

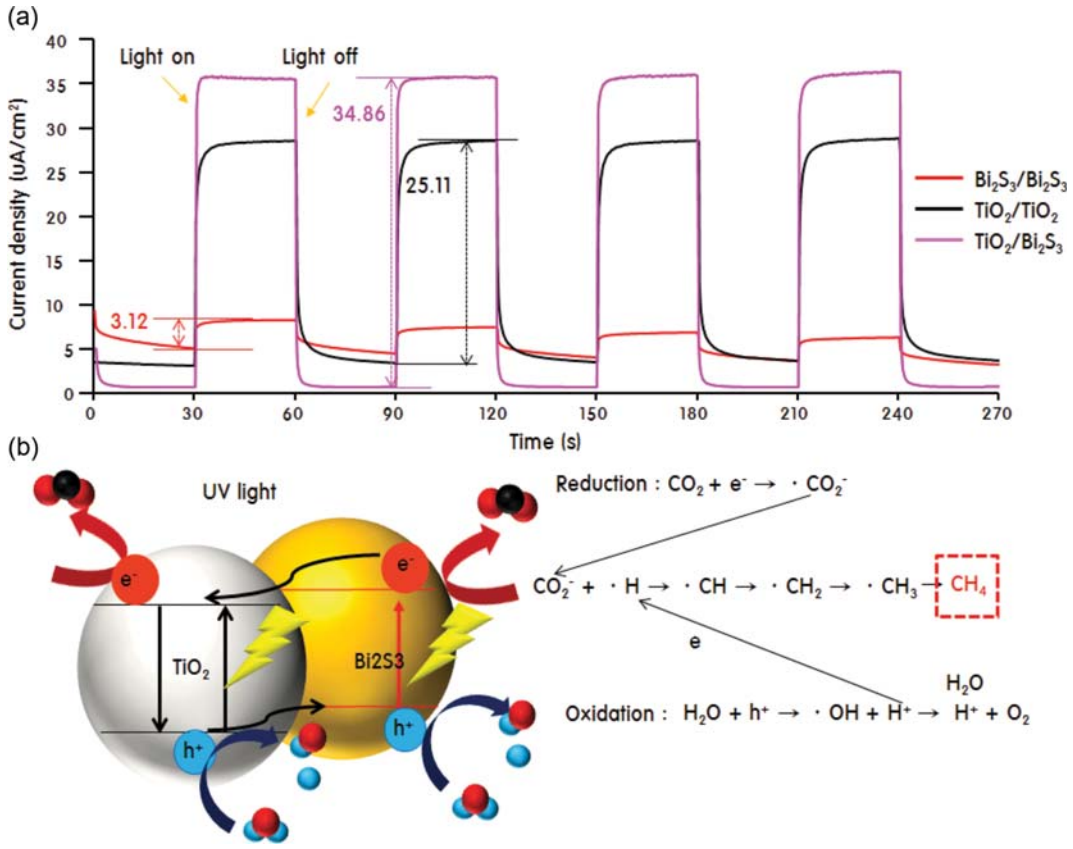

Fig. 11. Typical real-time photocurrent response (a) and an expected CO_2 photoreduction mechanism for reaction over TiO_2/Bi_2S_3 double-layered film.

trons are transferred from the VB to the CB, leaving a hole in the VB; this electron-hole pair is responsible for generation of the photocurrent [40]. Upon irradiation, the photoreduction current increases rapidly, and the photocurrent arrives a steady state after a few seconds. When irradiation is discontinued, the photocurrent instantaneously decreases to almost zero. The pure TiO_2/TiO_2 film exhibited a maximum photocurrent of 25.11 $mA \cdot cm^{-2}$, which is typical for extrinsic semiconductors. This behavior is typical of the surface photovoltage of n-type semiconductors, in which the positive charges move to the surface in the surface space-charge region [41]. On the other hand, the photoelectric signal corresponding to the sub-band transition of the Bi_2S_3/Bi_2S_3 film was too small, probably because the band-gap of Bi_2S_3 was small and the easily excited electrons appear to undergo fast recombination with the holes in the VB. Compared to the pure TiO_2/TiO_2 and Bi_2S_3/Bi_2S_3 films, the TiO_2/Bi_2S_3 film exhibited a higher photocurrent of about 34.86 $mA \cdot cm^{-2}$. From the XPS and UV-visible spectroscopic data, a mechanism was suggested for the photoreduction of CO_2 over the TiO_2/Bi_2S_3 double-layered film (Fig. 11(b)). The Bi_2S_3 particle has a short band-gap compared to that of pure TiO_2, and the CB and VB potential energies of Bi_2S_3 are located at higher levels compared to those of TiO_2. In the reaction over the fabricated TiO_2/Bi_2S_3 double-layered film, two types of electrons are captured by the CO_2 molecules. First, the electrons are rapidly and predominantly emitted from the VB to the CB of Bi_2S_3, which has a shorter band-gap, and the emitted electrons are then trapped by CO_2 molecules. The positive holes in the VB of the Bi_2S_3 top-layer can be trapped by OH^- or H_2O species. Secondly, the non-trapped electrons on the Bi_2S_3 top-layer can be transferred to the CB of the TiO_2 bottom-layer, resulting in a decrease in their recombination in the TiO_2/Bi_2S_3 double-layered film; therefore, the photoexcited electrons in the CB of the Bi_2S_3 top-layer are efficiently transferred to CO_2, thereby functioning as an efficient reducing agent. Consequently, these processes accelerate the separation of photogenerated electron-hole pairs (e^-/h^+) to promote the CO_2 reduction process, and enhance the catalytic performance.

CONCLUSIONS

Nano-sized Bi_2S_3 and TiO_2 were synthesized using a conventional sol-gel method for application as catalysts in CO_2 reduction. The XRD patterns of the Bi_2S_3 and TiO_2 powders corresponded to orthorhombic and anatase tetragonal structures, respectively, and TEM analysis of the prepared Bi_2S_3 and TiO_2 particles indicated a rod-like morphology with dimensions of 80-120 nm in length and 40 nm in width for the former and a spherical shape with a diameter of 10 nm for the latter. UV-visible spectroscopy and XPS analysis confirmed that the band-gaps of TiO_2 and Bi_2S_3 were 2.72 and 0.94 eV, respectively. Six types of double-layered dense films were fabricated using different coating sequences: TiO_2/TiO_2, Bi_2S_3/TiO_2, Bi_2S_3/Bi_2S_3, TiO_2/Bi_2S_3, TiO_2/Bi_2S_3 : TiO_2 (1 : 1) mix, and Bi_2S_3 : TiO_2 (1 : 1) mix/Bi_2S_3 : TiO_2 (1 : 1) mix; the films were applied to the

photoreduction of CO_2 to CH_4. The TiO_2/Bi_2S_3 film exhibited the best photocatalytic behavior, wherein 35.2 μmol·$g_{cat}^{-1}L^{-1}$ of CH_4 was produced after 10 h of reaction, and CO was generated as a secondary product by conversion of one-third of CH_4. The photoluminescence and photocurrent of the TiO_2/Bi_2S_3 double-layered film were, respectively, smaller and larger than those of the pure TiO_2/TiO_2 and Bi_2S_3/Bi_2S_3 films. Consequently, the TiO_2/Bi_2S_3 double-layered film promoted separation of the photogenerated electron-hole pairs (e^-/h^+), thereby accelerating the CO_2 reduction process and enhancing the catalytic performance. The results indicate that the TiO_2/Bi_2S_3 double-layered film is useful as a photocatalyst for the reduction of CO_2 to CH_4. Finally, this study presents one important fact: the enhanced catalytic activity of double-layered films is closely related to reliable coating techniques, especially for reproducible results. If the optimum coating thickness of the top layer can be evaluated and controlled, the lifetime of the electrons staying in the CB can be increased to prolong the lifetime of the catalyst and consequently the conversion of carbon dioxide to methane is significantly improved.

ACKNOWLEDGEMENTS

This work was supported by the Energy Efficiency and Resources Programs of the Korea Institute of Energy Technology Evaluation and Planning (KETEP), granted financial resources from the Ministry of Trade, Industry and Energy, Republic of Korea (20163010050080).

REFERENCES

1. C. M. Pittelkow, M. A. Adviento-Borbe, J. E. Hill, J. Six, C. van Kessel and B. A. Linquist, *Agric. Ecosysyst. Environ.*, **177**, 10 (2013).
2. T.-J. Kang, H. J. Park, H. N. Kung, L.-H. Xu, J.-H. Park, I. Heo, T.-S. Chang, B. S. Kim and H.-T. Kim, *Korean J. Chem. Eng.*, **34**, 2597 (2017).
3. P. Ziemkiewicz, P. H. Stauffer, J. Sullivan-Graham, S. P. Chu, W. L. Bourcier, T. A. Buscheck, T. Carr, J. Donovan, Z. Jiao, L. Lin, L. Song, J. L. Wagoner, *Tianjin PR China Int. J. Greenhouse Gas Control.*, **54**, 538 (2016).
4. J. H. Choi, Y. E. Kim, S. C. Nam, S. H. Yun, Y. I. Yoon and J.-H. Lee, *Korean J. Chem. Eng.*, **33**, 3222 (2016).
5. B. Lee and H. Lim, *Korean J. Chem. Eng.*, **34**, 199 (2017).
6. T. Yu, Q. Yuan, J. Lu, J. Ding and Y. Lu, *Appl. Energy*, **185**, 1994 (2017).
7. T. J. Erb and J. Zarzycki, *Curr. Opinion Chem. Biol.*, **34**, 72 (2016).
8. X. F. Lei, Z. N. Zhang, Z. X. Wu, Y. J. Piao, C. Chen, X. Li, X. X. Xue and H. Yang, *Sep. Purif. Technol.*, **174**, 66 (2017).
9. H. Senboku and A. Katayama, *Curr. Opinion Green Sustain. Chem.*, **3**, 50 (2017).
10. S. W. Jo, B. S. Kwak, K. M. Kim, J. Y. Do, N.-K. Park, S. O. Ryu, H.-J. Ryu, J.-I. Baek and M. Kang, *Appl. Surf. Sci.*, **355**, 891 (2015).
11. X. Li, J. Wen, J. Low, Y. Fang and J. Yu, *Sci. China Mater.*, **57**, 70 (2014).
12. H. Lee, B. S. Kwak, N.-K. Park, J.-I. Baek, H.-J. Ryu and M. Kang, *Appl. Surf. Sci.*, **393**, 385 (2017).
13. J. H. Lee, S.-I. Kim, S.-M. Park and M. Kang, *Ceram. Int.*, **43**, 1768 (2017).
14. X. Meng, Q. Yu, G. Liu, L. Shi, G. Zhao, H. Liu, P. Li, K. Chang, T. Kako and J. Ye, *Nano Energy*, **34**, 524 (2017).
15. C. V. Reddy, J. Shim and M. Cho, *J. Phys. Chem. Solid*, **103**, 209 (2017).
16. R. G. A. Garcia, C. A. M. Avendaño, M. Pal, F. P. Delgado and N. R. Mathews, *Mater. Sci. Semicon. Proc.*, **44**, 91 (2016).
17. Y. Sun, G. Li, J. Xu and Z. Sun, *Mater. Lett.*, **174**, 238 (2016).
18. H. Li, J. Yang, J. Zhang and M. Zhou, *Roy. Soc. Chem.*, **2**, 6258 (2012).
19. J. Kim and M. Kang, *Int. J. Photoenergy*, **37**, 8249 (2012).
20. W. Wu, Z. Wu, T. Yu, C. Jiang and W.-S. Kim, *Sci. Technol. Adv. Mater.*, **16**, 023501 (2015).
21. Y. Im, S. Kang, K. M. Kim, T. Ju, G. B. Han, N.-K. Park, T. J. Lee and M. Kang, *Int. J. Photoenergy*, **2013**, 452542 (2013).
22. S. Kumar, S. Sharma, S. Sood, A. Umar and S. K. Kansal, *Ceram. Int.*, **42**, 17551 (2016).
23. M. P. Deshpande, P. N. Sakariya, S. V. Bhatt, N. Garg, K. Patel and S. H. Chaki, *Mater. Sci. Semicon. Proc.*, **21**, 180 (2014).
24. A. Chaturvedi, M. P. Joshi, P. Mondal, A. K. Sinha and A. K. Srivastava, *Appl. Surf. Sci.*, **396**, 303 (2017).
25. M. Park, B. S. Kwak, S. W. Jo and M. Kang, *Energy Convers. Manage.*, **103**, 431 (2015).
26. J. Wang, Y. Xia, Y. Dong, R. Chen, L. Xiang and S. Komarneni, *Appl. Catal. B.*, **192**, 8 (2016).
27. D. K. Panesar and J. Francis, *Construct. Build. Mater.*, **52**, 52 (2014).
28. M. Khalfaoui, S. Knani, M. A. Hachicha and A. Ben Lamine, *J. Colloid Interface Sci.*, **263**, 350 (2003).
29. M. J. Ndolomingo and R. Meijboom, *Appl. Surf. Sci.*, **390**, 224 (2016).
30. M. Tahir and N. S. Amin, *Appl. Catal. B.*, **142-143**, 512 (2013).
31. A. Kubacka, M. J. Muñoz-Batista, M. Ferrer and M. Fernández-García, *Appl. Catal. B.*, **140-141**, 680 (2013).
32. K.-D. Jung and A. T. Bell, *J. Catal.*, **193**, 207 (2000).
33. Y. Yao and D. W. Goodman, *J. Mol. Catal. A.*, **383-384**, 239 (2014).
34. M. A. Asi, L. Zhu, C. He, V. K. Sharma, D. Shu, S. Li, J. Yang and Y. Xiong, *Catal. Today*, **216**, 268 (2013).
35. N. Singhal and U. Kumar, *Mol. Catal.*, **439**, 91 (2017).
36. H. Yu, J. Huang, H. Zhang, Q. Zhao and X. Zhong, *Nanotechnol.*, **25**, 215702 (2014).
37. T. Kato, Y. Hakari, S. Ikeda, Q. Jia, A. Iwase and A. Kudo, *J. Phys. Chem. Lett.*, **6**, 1042 (2015).
38. H. He, S. P. Berglund, P. Xiao, W. D. Chemelewski, Y. Zhang and C. B. Mullins, *J. Mater. Chem. A.*, **1**, 12826 (2013).
39. N. Farhangi, R. R. Chowdhury, Y. Medina-Gonzalez, M. B. Ray and P. A. Charpentier, *Appl. Catal. B.*, **110**, 25 (2011).
40. J. H. Lee, H. Lee and M. Kang, *Mater. Lett.*, **178**, 316 (2016).
41. S. S. Kalanur, Y. J. Hwang and O.-S. Joo, *J. Colloid Interface Sci.*, **402**, 94 (2013).